

Sky location of Massive Black Hole Binaries in the foreground of Galactic white dwarf binaries

Pan Guo^{1,4}, Hong-Bo Jin^{1,2,3,*}, Cong-Feng Qiao^{1,4}, and Yue-Liang Wu^{1,4,5}

¹*The International Centre for Theoretical Physics Asia-Pacific,*

University of Chinese Academy of Sciences, Beijing 100190, China

²*Institute for Frontiers in Astronomy and Astrophysics, Beijing Normal University, Beijing, China*

³*National Astronomical Observatories, Chinese Academy of Sciences, Beijing 100101, China*

⁴*The School of Physical Sciences, University of Chinese Academy of Sciences, Beijing 100049, China*

⁵*Institute of Theoretical Physics, Chinese Academy of Sciences, Beijing 100190, China*

(Dated: April 19, 2024)

Sky locating massive black hole binaries (MBHBs) from the foreground of double white dwarf (DWD) is essential for space-based gravitational wave (GW) detection. In an orbit period of the space crafts, there is an optimal orbital position of the GW detectors to observe GW sources, where the signal intensity is at its peak. From the model Q3-d, five MBHB sources are selected based on the optimal observation orbital positions of the GW detectors, which are associated with the orientation of the MBHB perpendicular to the detection arms. For two MBHB sources of lower intensity, luminosity distance uncertainties, $\Delta D_L/D_L$ at the 95% confidence level from the overlapping GW signals of MBHB and DWD sources, when employing wavelet decomposition and reconstruction methods, are improved by ~ 2 times. Besides, the angular resolutions $\Delta\Omega_s$ are also improved by a factor of ~ 20 . These results imply that we can obtain relatively high accuracy of quickly locating MBHB from the overlapped GW signals with DWDs at the best observation orbit position. The luminosity distance uncertainties at the 95% confidence level for MBHB sources with the higher sign-noise ratio, have constraints on the precision of the Hubble constant.

I. INTRODUCTION

During the O1-O3 observing runs, ground-based observatories from the LIGO, Virgo, and KAGRA collaborations[1, 2] have detected nearly one hundred gravitational wave events with frequency above 10 Hz. Gravitational wave detection from space-based observatories, such as LISA[3] and Taiji [4], operates in the low-frequency range, spanning from 10^{-4} to $10^{-1}Hz$. Gravitational wave (GW) signals emitted by the merger of massive black holes persist for an extended duration within the sensitive frequency band of space-based detectors, often overlapping with the continuous, nearly monochromatic GW signals produced by Galactic white dwarf binaries. The number of Galactic white dwarf binaries is in the order of 10^7 , and this type of source is also called the foreground signal[5, 6]. The number of resolvable foreground signals are about 10^4 [7, 8].

The identification of foreground signals remains a challenge in the detection of space-based gravitational waves. Overlapping gravitational wave (GW) sources can interfere with the detection of other signals, including those from merging massive black hole binaries[9]. The data analysis of those overlapping signals is one of the LISA Data Challenges[10] and the Taiji Data Challenge [11]. The data analysis of overlapped GW signals become already a general issue to be solved.

locating the sky position of the gravitational source is a key scientific goal for gravitational wave observations[12].

Quickly locating the identified binaries is the basic requirement for the space-based gravitational wave detection, that is used to calibrate the detection data and reduce the noises of detectors. Moreover, accurately determining the sky positions of these gravitational sources facilitates multi-messenger observations when combined with other gravitational wave detectors and astronomical data. Additionally, the uncertainty in the sky location parameter, specifically the luminosity distance, derived from these sources can contribute to refining the estimation of the Hubble constant within cosmological models through the distance-redshift relationship[13].

For the sky location methods of gravitational wave signals, there are mainly two types: One method is to use FIM (Fisher information matrix) to estimate the source parameter error, which can give the estimation of the spatial location of the gravitational source with high signal-to-noise ratio (SNR), and the inverse FIM gives the covariance matrix of the parameters. The angular resolution of the detector and the estimated signal parameters can also be calculated as a function of the spatial position and frequency of the source[14]. Different detectors of joint detection can effectively achieve better waves space positioning accuracy [15–18]. The parameter error estimation method of FIM is limited by the signal-to-noise ratio, and it is only a general error estimation of the detector's ability to locate the gravitational source.

The second kind of method is based on Bayesian method, the posterior distribution describes the uncertainty of the gravitational source parameters. The most successful of the bayesian approach is based on markov chain monte carlo (MCMC) methods [19–21], this kind of method provides richer information about the source

* Corresponding author Email: hbjin@bao.ac.cn

parameters, but compared with the second kind, the calculation cost is higher. However, the MCMC method is a classical algorithm for parameter estimation of gravitational sources. This method can realize the parameter estimation of space gravitational source completely.

In our previous work, see Reference[22] for details, the Taiji response function is expressed in the transverse-traceless gauge and calculated numerically in the time domain. We find that the amplitude of GW signals are modulated by the periodic motion of GW detectors on the solar orbit. The searching of GW signals and parameter estimation of GW sources from the experimental data of the space-based mission do not ignore the orbit positions relevant to GW sources.

In this paper, we focus on the sky location of massive black hole binaries from foreground of Galactic white dwarf binaries, considering the amplitude modulation effect of different detector positions on the detector response. The best observation based on short time of massive black hole binaries is achieved in this paper. Three models for the population of massive black hole binary, i.e., pop III, Q3-nod, and Q3-d[9], are considered to predict the events of massive black hole binary mergers. For some specific Q3-d sources, the best location the sky position of the sources at the best detector position is achieved in this paper. For the relatively strong Q3-d sources, the accuracy of the parameters obtained from overlapped signals is close to that without overlapped signals. However, for MBHB sources of lower intensity, the accuracy of the parameters obtained from overlapped signals is much worse than that without overlapped signals. The method of wavelet decomposition and reconstruction can significantly weaken the impact of overlapping with DWDs for MBHB sources of lower intensity.

The structure of this paper is as follows: in Sec. II, we mainly introduce the signal model of the MBHB and the DWDs sources; the detector response and the method used in this paper are shown in Sec. III, the detector response is presented and best orbit position for observation is obtained; in Sec. IV, Sky location of MBHB at the best detector position is achieved; in Sec. V, the full text is summarized.

II. SIGNAL MODEL

A. Massive Black Hole Binary

Three models for the population of MBHB, i.e., pop III, Q3-nod, and Q3-d[9], are considered to predict the events of MBHB mergers. The parameters are obtained from the website <https://www.gw-universe.org/obs-space.html>. The detector parameters are set as follows, see the table I for details.

We choose the model Q3-d that is closest to the reality among the three models, and 5 MBHB sources data is listed according to the time length of one year.

There are eight parameters: intrinsic mass of primary

/ secondary BH (M_\odot) $M1/M2$, cosmological redshift z , spin of primary/secondary BH $s1/2$, luminosity distance (Gpc) D_L , Ecliptic latitude (rad) β , Ecliptical longitude (rad) λ , and signal to noise ratio SNR. We select a higher-multipole gravitational waveform model for an eccentric binary black holes based on the effective-one-body-numerical-relativity formalism, waveform model SEOBNRE [23, 24]. In the simulation experiment in this paper, the deflection Angle ι is set to 60 degrees, and the polarization Angle ψ is set to 0. Specifically, 8 parameters are required, see the table II for details.

B. Galactic white dwarf binaries

For Taiji, since the band of space gravitational wave detection is ranging from 10^{-4} to $10^{-1} Hz$, a large number of Galactic white dwarf binaries are overlapped in this band, that is, Galactic foreground is formed. DWDs are described by a set of eight parameters: frequency f , frequency derivative \dot{f} , amplitude \mathcal{A} , sky position in ecliptic coordinates (λ, β) , orbital inclination ι , polarisation angle ψ , and initial phase ϕ_0 [25–27]. GWs emitted by a monochromatic source are characterized and quantified using the quadrupole approximation[28, 29]. In this approximation, the GW signal is described as a combination of the two polarizations (+ and \times):

$$h_+(t) = \mathcal{A}(1 + \cos \iota^2) \cos(\Phi(t)) \quad (1)$$

$$h_\times(t) = 2\mathcal{A} \cos \iota \sin(\Phi(t)) \quad (2)$$

with

$$\Phi(t) = 2\pi f t + \pi \dot{f} t^2 + \phi_0 \quad (3)$$

$$\dot{f} = \frac{96}{5} \pi^{8/3} \left(\frac{G\mathcal{M}}{c^3} \right)^{5/3} f^{11/3}, \quad (4)$$

$$\mathcal{A} = \frac{2(G\mathcal{M})^{5/3}}{c^4 D_L} (\pi f)^{2/3}, \quad (5)$$

where $\mathcal{M} \equiv (m_1 m_2)^{3/5} / (m_1 + m_2)^{1/5}$ is the chirp mass, and D_L is luminosity distance, and G and c are the gravitational constant and the speed of light, respectively.

The parameters of DWDs sources are obtained from the parameter distribution, which is detailed in the paper[22].

The coordinates under the *SSB*-frame are also composed of the spatial position coordinates (β, λ) . So we can calculate the amplitude of each DWDs signal source at each the spatial position coordinates (β, λ) from the DWDs in the Synthetic Galactic Population. The formula for calculating the amplitude is the Eq. 5. The latitude $(\beta \in [-\pi/2, \pi/2])$ is divided into 100 equal parts and the longitude $(\lambda \in [0, 2\pi])$ is divided into 100 equal

parameter	value	parameter	value
the Arm length[m]	3.0e9	the Laser pow[W]	2.2
Telescope diameter[m]	0.35	Acceleration Noise[Hz ⁻¹]	3.9e-44
Laser Shot Noise factor[Hz ⁻¹]	5.3e-38	Other Optical Metrology system noise [Hz ⁻¹]	2.81e-38
The Time [days]	365	SNR-threshold	8
Cosmology	FlatΛCDM-Planck15		

TABLE I. Parameter list of Detectors.

Q3-d	$M1 [M_\odot]$	$M2 [M_\odot]$	z	$D_L [\text{Gpc}]$	$\beta [\text{rad}]$	$\lambda [\text{rad}]$	SNR
Q3-delay-1	209156	27895	7.25	73.581	-0.06470	3.180	82.54
Q3-delay-2	1361322	770150	1.12	7.870	0.2066	4.536	1818
Q3-delay-3	1272097	1127338	1.69	12.986	-0.7767	3.965	3053
Q3-delay-4	389952	103676	5.54	53.903	-0.1365	0.7692	180.5
Q3-delay-5	103676	275282	0.749	4.758	0.1067	4.469	3661

TABLE II. Parameter list of model Q3-d.

parts. So we can get the grids of 100×100 on the sky map. Because there are so many of DWDs, there are many DWDs signals in each spatial grid. Here, we choose only the maximum value and keep its corresponding DWDs source as the source at that spatial location. So we can obtain ten thousand DWDs sources with larger amplitudes. Ten thousand DWDs sources are projected onto the detector arms (L_{12} , L_{23} , and L_{31}), the observation time is set to one year, and the sampling frequency is set to 0.1Hz. The polarisation angle is set $\psi = 0$, and initial orbital phase is set $\phi_0 = 0$. Finally, all the projection signals are added together to get the DWDs sources confusion signal. The time domain and frequency domain of the DWDs sources confusion signal on the detector arm L_{12} are as seen in Fig. 1.

C. Gravitational Wave Model

This is a source frame, but for detectors, a Solar System Barycenter (SSB) frame, based on the ecliptic plane is selected[30]. In the *SSB*-frame, the standard spherical coordinates (θ, ϕ) , and the associated spherical orthonormal basis vectors ($\mathbf{e}_r, \mathbf{e}_\theta, \mathbf{e}_\phi$) are confirmed. The position of the source in the sky will be parametrized by the ecliptic latitude $\beta = \pi/2 - \theta$ and the ecliptic longitude $\lambda = \phi$. The GW propagation vector \hat{k} in spherical coordinates is now

$$\hat{k} = -\mathbf{e}_r = -\cos \beta \cos \lambda \hat{\mathbf{x}} - \cos \beta \sin \lambda \hat{\mathbf{y}} - \sin \beta \hat{\mathbf{z}}. \quad (6)$$

Introduce reference polarization vectors as

$$\begin{aligned} \hat{u} &= -\mathbf{e}_\theta = -\sin \beta \cos \lambda \hat{\mathbf{x}} - \sin \beta \sin \lambda \hat{\mathbf{y}} + \cos \beta \hat{\mathbf{z}} \\ \hat{v} &= -\mathbf{e}_\phi = \sin \lambda \hat{\mathbf{x}} - \cos \lambda \hat{\mathbf{y}} \end{aligned} \quad (7)$$

The last degree of freedom between the frames corresponds to a rotation around the line of sight, and is represented by the polarization angle ψ . The polarization

tensors are given by

$$\begin{aligned} \epsilon^+ &= \cos(2\psi)\mathbf{e}^+ - \sin(2\psi)\mathbf{e}^\times \\ \epsilon^\times &= \sin(2\psi)\mathbf{e}^+ + \cos(2\psi)\mathbf{e}^\times, \end{aligned} \quad (8)$$

where the basis tensors \mathbf{e}^+ and \mathbf{e}^\times are expressed in terms of two orthogonal unit vectors,

$$\begin{aligned} \mathbf{e}^+ &= \hat{u} \otimes \hat{u} - \hat{v} \otimes \hat{v} \\ \mathbf{e}^\times &= \hat{u} \otimes \hat{v} + \hat{v} \otimes \hat{u}. \end{aligned} \quad (9)$$

GW traveling in the \hat{k} direction are written as the linear combination of two independent polarization states,

$$\mathbf{h}(\xi) = h_+(\xi)\epsilon^+ + h_\times(\xi)\epsilon^\times, \quad (10)$$

where the wave variable $\xi = t - \hat{k} \cdot \mathbf{x}$ gives the surfaces of constant phase.

III. SHORT-TIME OBSERVATION FROM TAIJI

A. Detector Response

Like LISA, the individual Taiji spacecraft will follow independent Keplerian orbits[31]. The spacecraft positions are expressed as a function of time. The parameter κ gives the initial ecliptic longitude. By setting the mean arm-length equal to those of the Taiji baseline, $L = 3 \times 10^9$ m.

The laser link signal is emitted from the spacecraft i at t_i moment and received by the spacecraft j at t_j moment. Assume that $c = 1$. The gravitational wave travels in the \hat{k} direction and $\mathbf{x}(t)$ is the position on the laser link at time t . The Eq. (11) can calculate the $\delta\ell_{ij}$ in a numerical way in the time domain[22].

$$\delta\ell_{ij} = \frac{1}{2} \hat{r}_{ij}(t) \otimes \hat{r}_{ij}(t) : \int_{t_i}^{t_j} \mathbf{h}(t - \hat{k} \cdot \mathbf{x}(t)) dt \quad (11)$$

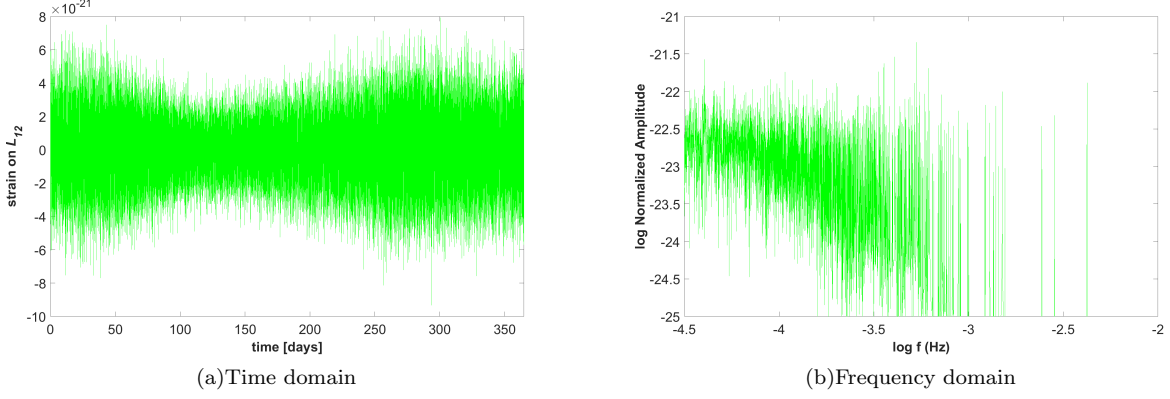


FIG. 1. The projection results on the detector L_{12} of DWDs confusion.

where, $\hat{r}_{ij}(t)$ denotes the unit vector

$$\hat{r}_{ij}(t_i) = \frac{\mathbf{x}_j(t_j) - \mathbf{x}_i(t_i)}{\ell_{ij}}. \quad (12)$$

and $\mathbf{h}(\xi)$ is the gravitational wave tensor in the transverse-traceless gauge. The colon here denotes a double contraction, $\mathbf{a} : \mathbf{b} = a^{ij}b_{ij}$.

B. Best orbit position for observation

The annual modulation effect of space gravitational wave detector on the source of gravitational wave is mainly the result of modulating the amplitude of the source signal. The annual modulation effect is mainly caused by the change of the Angle between the propagation direction of the gravitational wave (GW) source and the detector arm during the one-year orbit. In this case, we're defining the Angle θ [22]

$$\theta = \arccos \left| \frac{\hat{k} \cdot \hat{r}_{ij}}{|\hat{k}| |\hat{r}_{ij}|} \right| \quad (13)$$

where \hat{k} is the propagation direction of the GW source and $\hat{r}_{ij}(t)$ denotes the unit vector in the Eq. (12). Here, we set $t_i = 0s$ and $t_j = 10s$. When the laser has the same transmitting time and receiving time, the Angle θ is different when the detectors are at different orbital positions.

In the extreme case, when the Angle $\theta = 0^\circ$, the projection of the GW source on the detector arms (L_{12} , L_{23} , and L_{31}) is the smallest; when the Angle $\theta = 90^\circ$, the GW source is projected on the detector arms (L_{12} , L_{23} , and L_{31}) to the maximum. In this case, the variable, the initial ecliptic longitude κ in detector orbit, is selected to present the detector position.

However, the Angle θ can not vary from 0° to 90° for GW sources in the whole space for all the variable κ value ($\kappa \in [0, 2\pi]$). Due to the constraints of the detector configuration and orbit position, the modulation effect of the

source signal in the all-sky observation will be different. See more details in [22].

Here We select 5 MBHB sources from Q3-delay model, Q3-delay-1~Q3-delay-5 to observe the annual modulation effect of the detector on them. Here, take 365 different κ values uniformly in the interval $\kappa \in [0, 2\pi]$. The change of the Angle θ on L_{12} , L_{23} and L_{31} and the mean of Angle θ on L_{12} , L_{23} and L_{31} along with orbit position parameter κ for MBHB: Q3-delay-1~MBHB: Q3-delay-5, respectively are shown in Fig. 2.

For MBHB: Q3-delay-1, the Angle θ on L_{23} can vary from about 70° to 90° . However, the Angle θ on L_{12} and L_{31} can vary from about 20° to about 70° . In other words, the projection signal amplitude of MBHB: Q3-delay-1 on the L_{23} always maintains a relatively large, while the projection signal amplitude of MBHB: Q3-delay-1 on L_{12} or L_{31} decreases due to the influence of different detectors positions.

When processing the one-year observation data, we must pay more attention to the data segment with the largest projection amplitude of the GW source to be solved, which makes the estimation results of the source parameters more accurate. The mean of the Angle θ on L_{12} , L_{31} and L_{23} can synthesize the size change of the GW source on the three detector arms. When the mean value reaches the maximum, the corresponding orbit position parameter κ is the best observation position. Therefore, the best observation position of a MBHB source is obtained according to the variation of Angle θ for all the variable κ value ($\kappa \in [0, 2\pi]$). So we can get the best observation position κ of 5 MBHB sources.

According to the best observation position of MBHB sources, by projecting the 5 signals of the model Q3-d, three observation data on the detector arms for each MBHB are obtained. By combining the responses of 5 MBHB sources of model Q3-d with the 10,000 DWDs confusion signal responses, 5 segments of overlapped GW signals data containing MBHB are obtained.

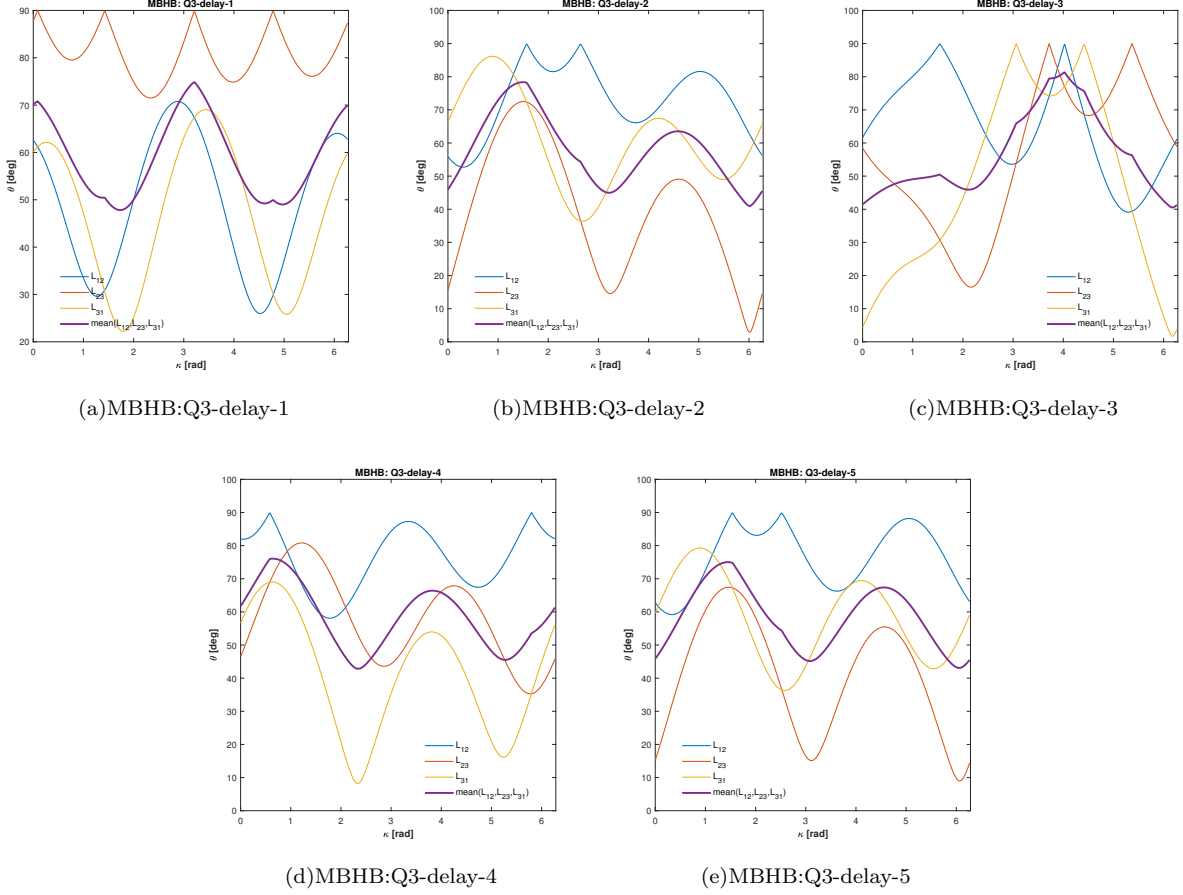


FIG. 2. The change of the Angle θ on L_{12} , L_{23} and L_{31} and the mean of Angle θ on L_{12} , L_{23} and L_{31} along with orbit position parameter κ for MBHB sources: Q3-delay-1~Q3-delay-5, respectively.

IV. SKY LOCATION OF MBHB

A. Bayesian inference

The Bayesian inference is based on calculating the posterior probability distribution function (PDF) of the unknown parameter set $\theta = \{\theta_1, \dots, \theta_m\}$ in a given model, which actually updates our state of belief from the prior PDF of θ after taking into account the information provided by the experimental data set D . The posterior PDF is related to the prior PDF by the Bayes's theorem

$$p(\theta|D) = \frac{\mathcal{L}(D|\theta)\pi(\theta)}{p(D)}, \quad (14)$$

where $\mathcal{L}(D|\theta)$ is the likelihood function, and $\pi(\theta)$ is the prior PDF which encompasses our state of knowledge on the values of the parameters before the observation of the data. The quantity $p(D)$ is the Bayesian evidence which is obtained by integrating the product of the likelihood and the prior over the whole volume of the parameter

space

$$p(D) = \int_V \mathcal{L}(D|\theta)\pi(\theta)d\theta. \quad (15)$$

The evidence is an important quantity for Bayesian model comparison. It is straight forward to obtain the marginal PDFs of interested parameters $\{\theta_1, \dots, \theta_n\}$ ($n < m$) by integrating out other nuisance parameters $\{\theta_{n+1}, \dots, \theta_m\}$

$$p(\theta_1, \dots, \theta_n)_{\text{marg}} = \int p(\theta|D) \prod_{i=n+1}^m d\theta_i. \quad (16)$$

The marginal PDF is often used in visual presentation. If there is no preferred value of θ_i in the allowed range $(\theta_{i,\min}, \theta_{i,\max})$, the priors are taken as a flat distribution

$$\pi(\theta_i) \propto \begin{cases} 1, & \text{for } \theta_{i,\min} < \theta_i < \theta_{i,\max} \\ 0, & \text{otherwise} \end{cases}. \quad (17)$$

The likelihood function is often assumed to be Gaussian

$$\mathcal{L}(D|\theta) = \prod_i \frac{1}{\sqrt{2\pi\sigma_i^2}} \exp \left[-\frac{(f_{\text{th},i}(\theta) - f_{\text{exp},i})^2}{2\sigma_i^2} \right], \quad (18)$$

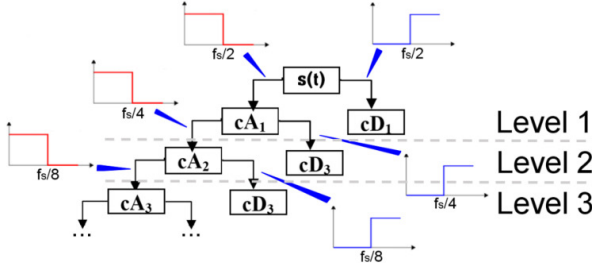


FIG. 3. Wavelet decomposition process of 3 level[36, 37].

where $f_{th,i}(\theta)$ are the predicted i -th observable from the model which depends on the parameter set θ , and $f_{exp,i}$ are the ones measured by the experiment with uncertainty σ_i .

When specifying the form of the likelihood function, a posterior PDF is determined using the Markov Monte Carlo (MCMC) method based on the prior PDF and likelihood function. Specifically, this article uses the Metropolis-Hastings sampling method to obtain a posterior PDF.

B. Wavelet decomposition and reconstruction

Wavelet transform (WT) [32–35] is a very important and classic method in signal processing. This article mainly studies the wavelet decomposition and reconstruction methods, and chooses the discrete wavelet transform (DWT) for calculation. First, downsample the object to be decomposed, and then perform wavelet decomposition of the signal. Through two different filters, namely high-pass and low-pass filters, convolved with the signal respectively, the coefficients after wavelet decomposition are obtained. It is divided into two types of coefficients, one is the detail coefficients (cD) obtained by high-pass filtering and the approximation coefficients (cA) obtained by the low-pass filter. The specific wavelet decomposition process is shown in the figure 3. Then select the detail coefficients (cD) and the approximation coefficients (cA) to obtain the reconstructed signal through wavelet reconstruction which is viewed as the inverse process of wavelet decomposition.

C. Posterior

The MBHB source position parameters are set by $\theta = \{\sin\beta, \lambda, D_L\}$. The prior is selected as the area near the true parameter values of 5 sources to be observed. Considering the program running time, for this experiment we selected 1 MCMC chain with a sample number of 136000, and calculated the log likelihood value for each group of samples. Then the posterior distribution of the parameters is obtained through the Metropolis-Hastings sampling method.

In this paper, three sets of comparisons are carried out. The first set is to solve the independent sources Q3-delay-1~Q3-delay-5 directly by FFT of their response data, abbreviated as MBHB(FFT); The second set is to solve the overlapped GW signals of Q3-delay-1~Q3-delay-5 and DWDs by FFT directly on their response data, abbreviated as MBHB+DWDs(FFT). The third set is to perform wavelet decomposition on the response data of the overlapped GW signals of Q3-delay-1, Q3-delay-4 and DWDs, and then perform FFT solution on the new data reconstructed after filtering the approximate coefficients, abbreviated as MBHB+DWDs(DWT+FFT). Here, $level = 6$ and $db6$ is selected for wavelet type of DWT.

Here, taking the χ^2 logarithm of the likelihood function gives the following form:

$$\chi^2 = \frac{(h_{th,i}(\theta) - h_{exp,i})^2}{\sigma_i^2}, \quad (19)$$

This paper mainly studies the observation results of the detector's three arms L_{12} , L_{23} and L_{31} . Therefore, in the Eq. (19), i values are 1, 2 and 3, corresponding to the projection of the GW source on the three detector arms respectively. The projected data obtained from the GW source to be solved at the best observation position is selected as the experimental data $h_{exp,i} = h_{MBHB,i}$ for MBHB(FFT) and $h_{exp,i} = h_{MBHB,i} + h_{DWDs,i}$ for MBHB+DWDs(FFT). The uncertainty of the experimental data $\sigma_i = 1/\text{SNR}_1 \times h_{MBHB,i}$ for MBHB(FFT) and $\sigma_i = 1/\text{SNR}_1 \times h_{MBHB,i} + 1/\text{SNR}_2 \times h_{DWDs,i}$ for MBHB+DWDs(FFT), where SNR_1 and SNR_2 are calculated by the Eq. (20) through the projected data obtained $h_{MBHB,i}$ and $h_{DWDs,i}$ and the analytic model for the sensitivity curve S_n , specifically formula (13)[38] for MBHB(FFT), adding formula (14)[38] to formula (13)[38] for MBHB+DWDs(FFT). The observation time $T_{OB} = 5 \times 10^5 s$. See details in the Table III.

$$\text{SNR}_{1,2} = \sqrt{\int \frac{|h_{MBHB,DWDs}^2(f)|}{S_n(f)} df}, \quad (20)$$

The specific posterior distributions of the first set and the second set of Q3-delay-2, Q3-delay-3 and Q3-delay-5 are shown in Figure 4. The specific posterior distributions of the first set, the second set and the third set of Q3-delay-1 and Q3-delay-4 are shown in the figure 5. The figure shows the one-dimensional and two-dimensional marginal posterior probability density distributions of the sky position parameters ($\sin\beta, \lambda, D_L$) of the source, and the best fitting values and statistical averages are obtained. The contour lines enclose the 68% and 95% probability regions of the parameter estimates. The black (blue) vertical line in the post-pdf of each one-dimensional marginal posterior PDF represents the true value (statistical mean). The black star (blue cross) in the pdf after each one-dimensional marginal posterior PDF represents the true value (statistical mean). The red

SNR	i	Q3-delay-1	Q3-delay-2	Q3-delay-3	Q3-delay-4	Q3-delay-5
SNR ₁ (MBHB)	1	4.9	326	362	22	366
	2	7.0	285	196	19	334
	3	5.2	248	258	22	282
SNR ₁ (MBHB+DWDs)	1	4.9	220	315	22	252
	2	4.9	155	141	18	233
	3	4.9	148	228	21	187
SNR ₂ (MBHB+DWDs)	1	1.0	2.4	1.9	4.6	2.4
	2	3.6	1.1	0.92	3.7	1.2
	3	0.76	2.8	1.6	1.3	3.0

TABLE III. SNR₁ and SNR₂ for MCMC of Q3-d sources. i are 1, 2, 3 corresponding to the detector's three arms L_{12} , L_{23} and L_{31} , respectively.

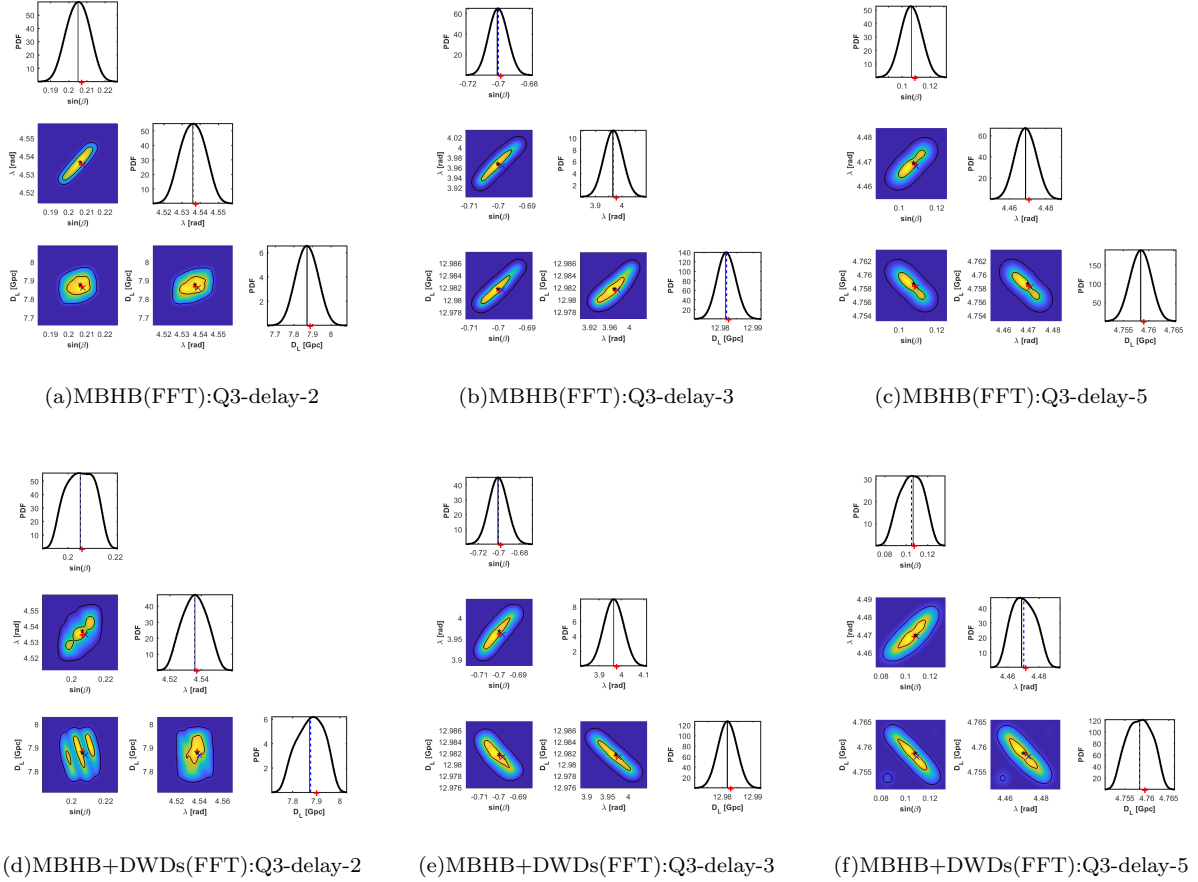


FIG. 4. The contract of posterior distribution of the sky position parameters ($\sin\beta$, λ , D_L) of MBHB(FFT) and MBHB+DWDs(FFT) for Q3-delay-2, Q3-delay-3 and Q3-delay-5. The black (blue) vertical line in the post-pdf of each one-dimensional marginal posterior PDF represents the true value (statistical mean). The black star (blue cross) in the pdf after each one-dimensional marginal posterior PDF represents the true value (statistical mean). The red plus sign in each one-dimensional and one-dimensional marginal posterior PDF indicates the best fit value. The contours contain the 68% and 95% probability regions of the parameter estimates.

plus sign in each one-dimensional and one-dimensional marginal posterior PDF indicates the best fit value. The contours contain the 68% and 95% probability regions of the parameter estimates.

The error in the solid angle [12] is given by,

$$\Delta\Omega_s = 2\pi \cos\beta \sqrt{C_{\beta\beta}C_{\lambda\lambda} - C_{\beta\lambda}^2} \quad (21)$$

The covariance matrix C is calculated from the posterior distribution of the parameters β and λ .

Table IV shows the results of parameter estimation of Q3-delay-1~Q3-delay-5. The sky location parameters and corresponding true values, the confidence interval at 68% and 95% confidence level, luminosity distance uncertainty, $\Delta D_L/D_L$ based on 95% confidence level and angular resolution $\Delta\Omega_s$ are shown in this table.

From the Figure 4, Figure 5 and Table IV, we can find that, for the relatively stronger MBHB sources, such as Q3-delay-2, Q3-delay-3, and Q3-delay-5, comparing the first set MBHB(FFT) and the second set MBHB+DWDs(FFT), we find that at a 95% confidence level, the parameters derived from the second set MBHB+DWDs(FFT) are comparable to those obtained from the first set MBHB(FFT). However, for MBHB sources of lower intensity, such as Q3-delay-1 and Q3-delay-4, comparing the first set MBHB(FFT) and the second set MBHB+DWDs(FFT), we find that at a 95% confidence level, the parameters derived from the second set MBHB+DWDs(FFT) much worse than that the first set MBHB(FFT). For MBHB sources of lower intensity, luminosity distance uncertainties, $\Delta D_L/D_L$ derived at a 95% confidence level from the third set MBHB+DWDs(DWT+FFT), when employing wavelet decomposition and reconstruction methods, are improved by ~ 2 times compared to that from the second set MBHB+DWDs(FFT), corresponding to Q3-delay-1 and Q3-delay-4 respectively. The angular resolutions $\Delta\Omega_s$ derived from from the third set MBHB+DWDs(DWT+FFT), when employing wavelet decomposition and reconstruction methods, are improved by ~ 20 times compared to that from the second set MBHB+DWDs(FFT), corresponding to Q3-delay-1 and Q3-delay-4 respectively. The method of wavelet decomposition and reconstruction can significantly weaken the impact of overlapping with DWDs for MBHB sources of lower intensity.

V. CONCLUSIONS

The GW signals from MBHB merging linger for much longer in the detector sensitive band, which overlap with the continuous and nearly monochromatic GW signals of DWDs sources. The data analysis of overlapped GW signals become already a general issue to be solved. In this paper, we focus on locating the sky position of MBHB from overlapped GW signals with DWDs sources. In fact,

the amplitude of GW signals are modulated by the periodic motion of GW detectors on the solar orbit. For the first time, the effects of the periodic orbit position parameter of space-based laser interferometer detectors on the locating the sky position of MBHB are considered.

The model, Q3-d, for the population of massive black hole binary is selected. At the best orbit position, the observations of Q3-d sources are performed. Location parameter estimation of the five MBHB sources are performed using the Metropolis-Hastings MCMC method. In this paper, three sets of comparisons are carried out. The first set is to solve the independent sources Q3-delay-1~Q3-delay-5 directly by FFT of their response data, abbreviated as MBHB(FFT); The second set is to solve overlapped GW signals of Q3-delay-1~Q3-delay-5 and DWDs sources by FFT directly on their response data, abbreviated as MBHB+DWDs(FFT). The third set is to perform wavelet decomposition on the response data of overlapped GW signals of Q3-delay-1, Q3-delay-4 and DWDs sources, and then perform FFT solution on the new data reconstructed after filtering the approximate coefficients, abbreviated as MBHB+DWDs(DWT+FFT). Here, $level = 6$ and $db6$ is selected for wavelet type of DWT.

For the relatively stronger MBHB sources, such as Q3-delay-2, Q3-delay-3, and Q3-delay-5, comparing the first set MBHB(FFT) and the second set MBHB+DWDs(FFT), we find that at a 95% confidence level, the parameters derived from the second set MBHB+DWDs(FFT) are comparable to those obtained from the first set MBHB(FFT). However, for MBHB sources of lower intensity, such as Q3-delay-1 and Q3-delay-4, comparing the first set MBHB(FFT) and the second set MBHB+DWDs(FFT), we find that at a 95% confidence level, the parameters derived from the second set MBHB+DWDs(FFT) much worse than that the first set MBHB(FFT). The method of wavelet decomposition and reconstruction is used in the paper.

For MBHB sources of lower intensity, luminosity distance uncertainties, $\Delta D_L/D_L$ derived at a 95% confidence level from the overlapping GW signals of MBHB and DWD sources, when employing wavelet decomposition and reconstruction methods, are improved by a factor of ~ 2 , corresponding to Q3-delay-1 and Q3-delay-4 respectively. The angular resolutions $\Delta\Omega_s$ derived from from the third set MBHB+DWDs(DWT+FFT), when employing wavelet decomposition and reconstruction methods, are improved by ~ 20 times compared to that from the second set MBHB+DWDs(FFT), corresponding to Q3-delay-1 and Q3-delay-4 respectively. The method of wavelet decomposition and reconstruction can significantly weaken the impact of overlapping with DWDs for MBHB sources of lower intensity.

The angular resolution $\Delta\Omega_s$ and luminosity distance uncertainty, $\Delta D_L/D_L$ of the method based on a short observation time are smaller than the ones in [15] based on observation time of about 10 days. Through the distance-redshift relation, the luminosity distance uncertainty

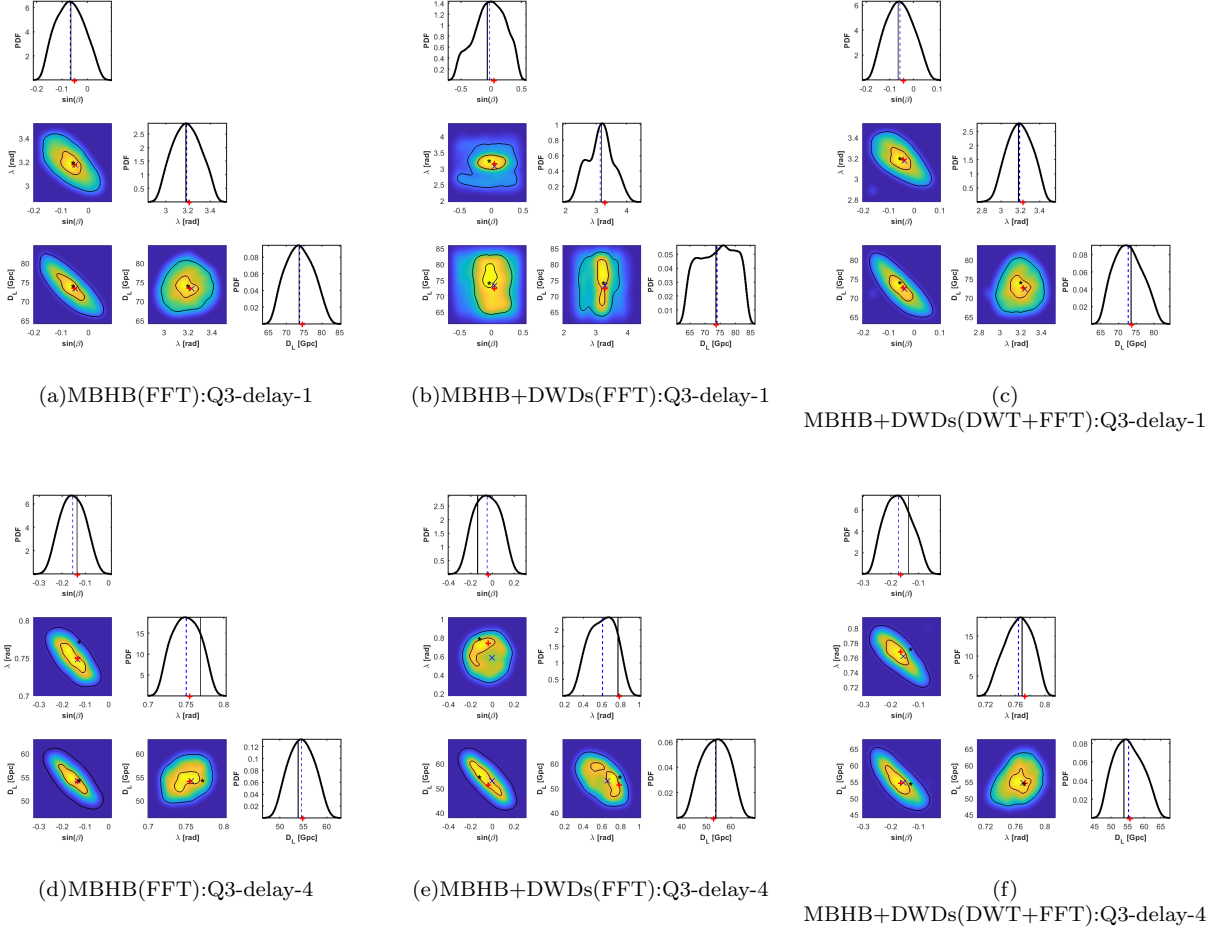


FIG. 5. The contract of posterior distribution of the sky position parameters of MBHB(FFT), MBHB+DWDs(FFT) and MBHB+DWDs(DWT+FFT) for Q3-delay-1 and Q3-delay-4. The black (blue) vertical line in the post-pdf of each one-dimensional marginal posterior PDF represents the true value (statistical mean). The black star (blue cross) in the pdf after each one-dimensional marginal posterior PDF represents the true value (statistical mean). The red plus sign in each one-dimensional and one-dimensional marginal posterior PDF indicates the best fit value. The contours contain the 68% and 95% probability regions of the parameter estimates.

obtained by gravitational source can help constrain the accuracy of the Hubble constant in cosmology[13]. $\lg(\Delta D_L/D_L)$ at 95% confidence level of Q3-delay-3 and Q3-delay-5 for Taiji is lower than that for ET2CE[13] which is about -2 and $\lg(\Delta D_L/D_L)$ at 95% confidence level of Q3-delay-2 for Taiji is lower than that for ET[13] which is about -1.5 . The luminosity distance uncertainty at 95% confidence level obtained by MBHB based on the method in this paper can enhance the constraints on the accuracy of the Hubble constant in cosmology.

ACKNOWLEDGEMENTS

This work has been supported by the Fundamental Research Funds for the Central Universities. This work

has been supported in part by the National Key Research and Development Program of China under Grant No.2020YFC2201500, the National Science Foundation of China (NSFC) under Grants Nos. 12147103, 11821505, 11975236, and 12235008, the Strategic Priority Research Program of the Chinese Academy of Sciences under Grant No. XDB23030100. In this paper, The numerical computation of this work was completed at TAIJI Cluster of University of Chinese Academy of Sciences.

Q3-d	three sets of comparisons	parameter	real value	95% CL	$\lg(\Delta D_L/D_L)$	$\lg(\Delta\Omega_s[deg^2])$
Q3-delay-1	MBHB(FFT)	D_L [Gpc]	73.58	[66.81, 80.73]	-0.7231	1.996
		$\sin\beta$	-0.06466	[-0.1669, 0.03313]		
		$\lambda[deg]$	182.2	[169.7, 195.8]		
	MBHB+DWDs(FFT)	D_L [Gpc]	73.58	[59.7, 89.16]	-0.3975	3.352
		$\sin\beta$	-0.06466	[-0.5422, 0.4818]		
		$\lambda[deg]$	182.2	[129.2, 230.3]		
	MBHB+DWDs(DWT+FFT)	D_L [Gpc]	73.58	[65.64, 79.96]	-0.7108	2.049
		$\sin\beta$	-0.06466	[-0.1629, 0.04774]		
		$\lambda[deg]$	182.2	[169.1, 196.6]		
Q3-delay-2	MBHB(FFT)	D_L [Gpc]	7.870	[7.780, 7.960]	-1.640	-0.7395
		$\sin\beta$	0.2051	[0.1955, 0.2147]		
		$\lambda[deg]$	259.9	[259.3, 260.5]		
	MBHB+DWDs(FFT)	D_L [Gpc]	7.870	[7.767, 7.987]	-1.553	-0.3367
		$\sin\beta$	0.2051	[-0.2358, -0.04041]		
		$\lambda[deg]$	259.9	[259.1, 260.7]		
Q3-delay-3	MBHB(FFT)	D_L [Gpc]	12.98	[12.97, 12.99]	-2.812	-0.4672
		$\sin\beta$	-0.7009	[-0.7122, -0.6886]		
		$\lambda[deg]$	227.2	[223.4, 231.2]		
	MBHB+DWDs(FFT)	D_L [Gpc]	12.98	[12.97, 12.99]	-2.812	0.009341
		$\sin\beta$	-0.7009	[-0.7177, -0.6837]		
		$\lambda[deg]$	227.2	[222.4, 231.9]		
Q3-delay-4	MBHB(FFT)	D_L [Gpc]	53.90	[49.61, 59.63]	-0.7307	1.044
		$\sin\beta$	-0.1361	[-0.2527, -0.05645]		
		$\lambda[deg]$	44.07	[41.13, 44.87]		
	MBHB+DWDs(FFT)	D_L [Gpc]	53.90	[43.7, 63.68]	-0.431	2.464
		$\sin\beta$	-0.1361	[-0.2619, 0.1651]		
		$\lambda[deg]$	44.07	[19.84, 49.42]		
	MBHB+DWDs(DWT+FFT)	D_L [Gpc]	53.90	[47.57, 62.95]	-0.5447	1.051
		$\sin\beta$	-0.1361	[-0.2608, -0.08463]		
		$\lambda[deg]$	44.07	[41.86, 45.71]		
Q3-delay-5	MBHB(FFT)	D_L [Gpc]	4.758	[4.748, 4.768]	-2.376	-1.125
		$\sin\beta$	0.1065	[0.0923, 0.1207]		
		$\lambda[deg]$	256	[255.4, 256.7]		
	MBHB+DWDs(FFT)	D_L [Gpc]	4.758	[4.748, 4.768]	-2.376	-0.1817
		$\sin\beta$	0.1065	[0.08503, 0.125]		
		$\lambda[deg]$	256	[255.3, 256.9]		

TABLE IV. The results of three sets of comparisons of sky location parameter estimation of Q3-delay-1~Q3-delay-5. Three sets of comparisons are given in column 2. The spatial position parameters and their true values are given in column 3. The confidence interval and luminosity distance uncertainty, $\Delta D_L/D_L$ based on 95% confidence level are given in column 4. The angular resolution $\Delta\Omega_s$ is shown in column 5.

-
- [1] R. Abbott, T. Abbott, F. Acernese, K. Ackley, C. Adams, N. Adhikari, R. Adhikari, V. Adya, C. Affeldt, D. Agarwal, et al., Physical Review X **13**, 041039 (2023).
- [2] R. Abbott, H. Abe, F. Acernese, K. Ackley, S. Adhikari, N. Adhikari, R. Adhikari, V. Adkins, V. Adya, C. Affeldt, et al., arXiv preprint arXiv:2302.03676 (2023).
- [3] P. Amaro-Seoane, H. Audley, S. Babak, J. Baker, E. Barausse, P. Bender, E. Berti, P. Binetruy, M. Born, D. Bottoluzzi, et al., arXiv preprint arXiv:1702.00786 (2017).
- [4] W.-R. Hu and Y.-L. Wu, *The taiji program in space for gravitational wave physics and the nature of gravity* (2017).
- [5] A. J. Farmer and E. S. Phinney, Monthly Notices of the Royal Astronomical Society **346**, 1197 (2003).
- [6] G. Nelemans, Classical and Quantum Gravity **26**, 094030 (2009).
- [7] T. B. Littenberg, N. J. Cornish, K. Lackeos, and T. Robson, Phys. Rev. D **101**, 123021 (2020), URL <https://link.aps.org/doi/10.1103/PhysRevD.101.123021>.

- [8] X.-H. Zhang, S. D. Mohanty, X.-B. Zou, and Y.-X. Liu, *Physical Review D* **104**, 024023 (2021).
- [9] A. Klein, E. Barausse, A. Sesana, A. Petiteau, E. Berti, S. Babak, J. Gair, S. Aoudia, I. Hinder, F. Ohme, et al., *Physical Review D* **93**, 024003 (2016).
- [10] *LISA Data Challenge*, <https://lisa-ldc.lal.in2p3.fr/>.
- [11] *Taiji Data Challenge*, <http://taiji-tdc.ictp-ap.org/>.
- [12] A. Blaum, *Physical Review D* **83**, 083006 (2011).
- [13] J.-Y. Song, L.-F. Wang, Y. Li, Z.-W. Zhao, J.-F. Zhang, W. Zhao, and X. Zhang, *Science China Physics, Mechanics & Astronomy* **67** (2024), ISSN 1869-1927, URL <http://dx.doi.org/10.1007/s11433-023-2260-2>.
- [14] L. Wen and Y. Chen, *Physical Review D - Particles, Fields, Gravitation and Cosmology* **81**, 1 (2010), ISSN 15507998.
- [15] W.-H. Ruan, C. Liu, Z.-K. Guo, Y.-L. Wu, and R.-G. Cai, *Research* **2021**, 1 (2021), URL <https://doi.org/10.34133/2F2021%2F6014164>.
- [16] R. Wen-Hong, C. Liu, G. Zong-Kuan, W. Yue-Liang, and C. Rong-Gen, *Nature Astronomy* **4**, 108 (2020).
- [17] G. Wang, W. T. Ni, W. B. Han, S. C. Yang, and X. Y. Zhong, *Physical Review D* **102**, 1 (2020), ISSN 24700029, 2002.12628.
- [18] C. Zhang, Y. Gong, H. Liu, B. Wang, and C. Zhang, *Physical Review D* **103** (2021), URL <https://doi.org/10.1103/2Fphysrevd.103.103013>.
- [19] J. Crowder and N. J. Cornish, *Physical Review D* **75**, 043008 (2007).
- [20] J. Crowder and N. J. Cornish, *Classical and Quantum Gravity* **24**, S575 (2007).
- [21] T. B. Littenberg, *Physical Review D* **84**, 063009 (2011).
- [22] P. Guo, H.-B. Jin, C.-F. Qiao, and Y.-L. Wu, *Results Phys.* **60**, 107607 (2024), 2310.16796.
- [23] Z. Cao and W.-B. Han, *Physical Review D* **96**, 044028 (2017).
- [24] X. Liu, Z. Cao, and Z.-H. Zhu, *Classical and Quantum Gravity* **39**, 035009 (2022).
- [25] C. Cutler, *Physical Review D* **57**, 7089 (1998).
- [26] E. Roebber, R. Buscicchio, A. Vecchio, C. J. Moore, A. Klein, V. Korol, S. Toonen, D. Gerosa, J. Goldstein, S. M. Gaebel, et al., *The Astrophysical Journal Letters* **894**, L15 (2020).
- [27] N. Karnesis, S. Babak, M. Pieroni, N. Cornish, and T. Littenberg, *Physical Review D* **104**, 043019 (2021).
- [28] L. D. Landau and E. M. Lifshitz, *The classical theory of fields; 2nd ed.* (Pergamon, 1962), URL <https://cds.cern.ch/record/101809>.
- [29] P. C. Peters and J. Mathews, *Physical Review* **131**, 435 (1963).
- [30] Note1, <https://lisa-ldc.lal.in2p3.fr/static/data/pdf/LDC-manual-002.pdf>.
- [31] L. J. Rubbo, N. J. Cornish, and O. Poujade, *Physical Review D* **69**, 082003 (2004).
- [32] C. K. Chui, *An introduction to wavelets*, vol. 1 (Academic press, 1992).
- [33] I. Meyer et al., *Wavelets and applications*, vol. 31 (Masson Paris, 1992).
- [34] J. J. Benedetto, *Wavelets: mathematics and applications*, vol. 13 (CRC press, 1993).
- [35] M. Misiti, Y. Misiti, G. Oppenheim, and J.-M. Poggi, *Wavelets and their Applications* (John Wiley & Sons, 2013).
- [36] P. Wodarski, J. Jurkojć, and M. Gzik, *Sensors* **20** (2020), ISSN 1424-8220, URL <https://www.mdpi.com/1424-8220/20/24/7138>.
- [37] P. Singh, P. Singh, and R. K. Sharma, *International Journal of Computer Applications* **13**, 1 (2011).
- [38] T. Robson, N. J. Cornish, and C. Liu, *Classical and Quantum Gravity* **36**, 105011 (2019).